Experimental investigation of the alternate recurrence of quasi-static and dynamic crack propagation in PMMA

Raphael Heinzmann, Rian Seghir, Syed Yasir Alam, Julien Réthoré

Noname manuscript No.
(will be inserted by the editor)

Experimental investigation of the alternate recurrence of quasi-static and dynamic crack propagation in PMMA.

Raphael Heinzmann · Rian Seghir · Syed Yasir Alam · Julien Réthoré

Received: / Accepted:

Abstract The alternate (stick-slip) cracking phenomenon in Poly(methyl methacrylate) (PMMA) was investigated using high-speed imaging and digital image correlation (DIC). PMMA is known to show a great variety of fracture behaviors by even small changes in loading conditions. With TDCB-shaped samples and under a range of constant extension rates, the phenomenon of alternate cracking is observed. Here, loops of successive quasi-static and dynamic crack propagation are found within a single fracture experiment suggesting a 'forbidden' velocity regime. For the first time, such material/structural cyclic fracture behavior is examined through the lens of linear elastic fracture mechanics (LEFM) by using in-situ High-Speed (HS) DIC. Energy release rates and crack velocities during fracture experiments are derived from full-field measurements using Williams' series expansion. Fracture surfaces of post-mortem samples have been systematically analyzed using optical microscopy. The investigation of the actual limits of the 'forbidden' velocity regime in terms of critical velocity and energy release rate in relation to post-mortem crack length features is achieved by holistic experimental data on alternate cracking. This work provides key experimental data regarding the improved understanding of a unified theoretical framework of crack instabilities.

Keywords Polymers · Fracture Mechanics · High Speed DIC · Stick-Slip · 'Forbidden' Velocity

Raphael Heinzmann
Nantes Université, Ecole Centrale Nantes, CNRS, GeM, UMR 6183, F-44000, Nantes, France
E-mail: raphael.heinzmann@ec-nantes.fr

Rian Seghir
Nantes Université, Ecole Centrale Nantes, CNRS, GeM, UMR 6183, F-44000, Nantes, France
E-mail: rian.seghir@ec-nantes.fr

Syed Yasir Alam
Nantes Université, Ecole Centrale Nantes, CNRS, GeM, UMR 6183, F-44000, Nantes, France
E-mail: syed-yasir.alam@ec-nantes.fr

Julien Réthoré
Nantes Université, Ecole Centrale Nantes, CNRS, GeM, UMR 6183, F-44000, Nantes, France
E-mail: julien.rethore@ec-nantes.fr

1 Introduction

Even the failure of the smallest structural component can be the source of the global collapse of an entire engineering structure with severe consequences. Thus, understanding the mechanisms of failure by studying the formation and propagation of cracks is of utter importance in preventing such damaging events. A crucial parameter in fracture mechanics for experimental investigations of crack propagation is the crack velocity, as they are strongly related to underlying fracture mechanisms. In brittle materials, a wide range of velocities can already be explored by relatively minor variations in loading conditions. Within this span of observable velocities, two independent groups of interest—slow (quasi-static) and fast (dynamic) cracking—are covered in literature. Without considering impact tests, at very large constant extension rates, cracks typically propagate at very high velocities (about 0.5 times the Rayleigh wave speed) (Dally et al., 1985; Miller et al., 1999; Scheibert et al., 2010). In that case, cracks are considered unstable, which means that no additional load is required to significantly propagate the crack, eventually resulting in total failure of the sample. On the contrary, with a sufficiently slow loading rate, the crack propagates continuously stable with velocities at least two order of magnitude slower (Marshall et al., 1974; Beaumont and Young, 1975; Vasudevan et al., 2021). Between these two regimes, the phenomenon of alternate cracking (Ravi-Chandar and Balzano, 1988; Hattali et al., 2012) is observed for some materials. Even though the crack is driven by a constant extension rate, the two unique cracking behaviors can be found within one fracture experiment. Between these two propagation types, a range of velocities is suggested that can not be exploited by the crack. This causes a gap between the two well-defined phases of quasi-static and dynamic propagation that is commonly described as 'forbidden' velocity regime. Due to experimental (crack velocity mismatch of about two orders of magnitude) and theoretical considerations (apparent theoretical mismatch regarding the mechanisms), these two regimes have been investigated individually up to now. As a consequence, the 'forbidden' velocity regime has only been approached from both sides without clearly quantifying energies and velocities involved during transitions. The experimental design in this work however allows the investigation of the reoccurring appearance of the two particular crack propagation types during one fracture process in PMMA. Better estimations of the 'forbidden' velocity regime, considering in-process viscous effects (history-dependent), can be accomplished. Thus, to achieve improved velocity measurements through high temporal and moderate spatial resolution, up to date high-speed imaging has been employed. Energy release rate estimations benefit from direct measurements of crack tip positions and linear elastic fracture mechanic (LEFM) parameters through full-field measurements using digital image correlation (DIC) and Williams' series expansion.

The presented work is introduced with a brief description of the theoretical background and existing literature mainly regarding the experimental exploration of alternate cracking. In the following, relevant information related to the experimental program including short technical explanations of DIC and Williams' series expansion is presented. The work is then concluded by discussing the results of multiple TDCB experiments and a summary of the presented study.

2 Alternate (stick-slip) cracking

Beforehand, different terminologies are found in literature discussing this fracture phenomenon. The most commonly used expression is stick-slip, due to the theoretical proximity with observations during the frictional phenomenon of sliding (Feeny et al., 1998). In this study, however, alternate cracking is used to additionally specify and separate between sliding and fracture related observations.

2.1 Basic theoretical background

The specific behavior for materials showing alternate cracking is classically described by the kinematic law of brittle fracture in the space of energy release rate (G) as a function of the crack velocity (v) in the log-scale (Figure 1).

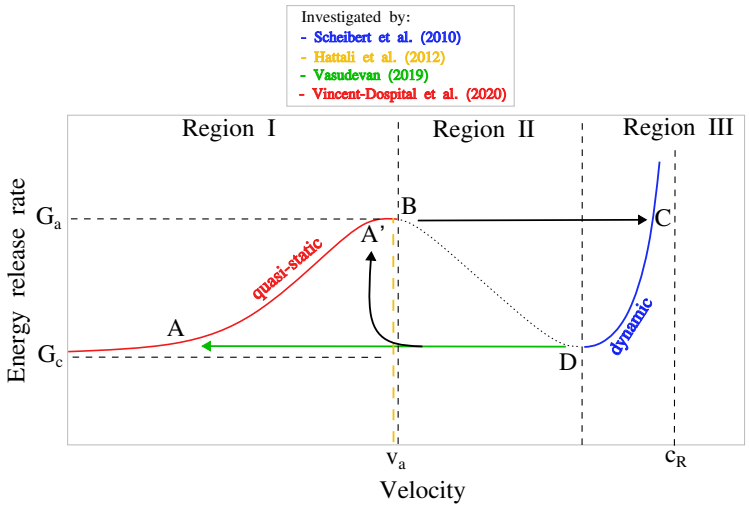

Fig. 1: Kinetic law (G_c-log v curve) for materials showing alternate cracking (stick-slip) behavior.

This kinematic law can be subdivided into three regions. Region I depicts a quasi-static propagation phase in which the Griffith criterion (Griffith, 1921) should apply. However, when varying the crack velocity over decades, it has been observed experimentally that the critical energy release rate actually depends on the crack velocity. Consequently, in this region, the crack speed is driven by its relationship with the critical energy release rate that varies between G_c for infinitely low crack speeds and avalanche threshold G_a at the transition with region II (A $\longrightarrow$ B). Extreme crack tip accelerations take place during the following region II with a supposedly "softening" branch causing the jump from the region I to the dynamic region III (B $\longrightarrow$ C). Hereinafter, the crack finds itself in the dynamic region where the generic Kanninen's relationship ($K_{ID} = K_{IC}/(1-(v/c_R)^m)$ with the dynamic SIF K_{ID}, static SIF K_{IC}, crack tip velocity v, Rayleigh wave speed c_R and material constant m) of dynamic fracture (Kanninen and

Popelar, 1985) can be applied, and crack tip speeds are restricted by the dynamic limiting speed of Rayleigh wave speed (c_R). However, during the high-velocity branch (region III), crack tip speeds in alternate cracking slow down after a certain propagation length to a point of arrest. This arrest marks the beginning of the second jump back to the slow velocity branch. For this, authors in existing literature generally propose the crack to follow along the reference points D to A. All this, due to the reiterating behavior, explains the appearance of a hysteresis implying a 'forbidden' velocity zone (between v^B and v^D).

A typical example of a fracture surface linked to such cracking is shown in Figure 2. Here, the two particular surface markings related to quasi-static and dynamic propagating cracks can be observed.

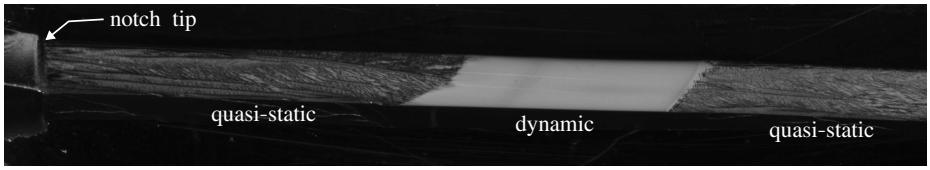

Fig. 2: Crack surface recorded with an inclined high resolution camera through the bulk of a transparent PMMA specimen visualizing the two phases of alternate cracking.

2.2 Existing literature

While regions I and III are being well defined and investigated independently, insufficient experimental data and few modeling attempts are provided in the literature to fuse the two regions with a proper description of the 'forbidden' region II. In the following, by focusing on the most recent modeling attempt and presented experimental methods, existing literature on alternate cracking will be presented briefly.

Most recently, (Vincent-Dospital et al., 2020) provided a predictive model of the fracturing behavior in PMMA based on the theoretical concept of thermal softening. In this model, the failure process is thermally activated and combined with the dissipation and diffusion of heat in the process zone surrounding the crack tip. Covering the vast range of different crack tip speeds found in PMMA fracturing, their thermodynamic approach showed good compliance with the experimental data of quasi-static and dynamic fracturing experiments. Furthermore, the two well-defined 'stable' regimes were connected by the model through a continuous description of the 'softening' branch. Noteworthily, no experimental data of alternate cracking was considered. Notice, for terminology purpose, that this unified model introduces the concept of sub-critical failure. Indeed, contrary to the discussion made around Figure 1, where velocity domains where classified through a discontinuous transition from classical Griffith theory to Kanninen's type rate dependent relationship, the authors propose that the actual critical energy released rate is reached at high velocity ($\sim$165 m.s^{-1}), while initiation and propagation at lower speed is supposedly sub-critical.

To this day, different methods have been used to experimentally investigate the phenomenon of alternate cracking. In the work of (Ravi-Chandar and Balzano, 1988), PMMA and Homalite-100 fracturing of single-edge-notched (SEN) and compact tension (CT) specimens were investigated by focusing on the temporal evolution of the

stress intensity factor. Stress intensity factor (SIF) data has been obtained through the method of caustics (Beinert and Kalthoff, 1981) using a camera system at 12 kfps over a duration of one minute. Crack length and K_I measurements were retrieved during quasi-static propagation phases of alternate cracking experiments, while the experimental setup did not support dynamic phase measurements.

(Hattali et al., 2012) investigated the phenomenon in PMMA, by focusing on crack tip speeds and fracture surfaces, using a high-resolution camera (maximal temporal and spatial resolution of 396 fps and 21 Mpix, respectively) and an in-house image processing tool. The system setup only allowed for the investigation of quasi-static crack propagation phases. Thus, only the lower limit of the 'forbidden' velocity regime, i.e. v_a, was investigated and found to be 3.5 cm.s^{-1} and 4.0 cm.s^{-1} for the two observed dynamic bursts, respectively. However, with an interframe of approx. 2.5 ms, it has to be expected that phase transitional velocities were not captured accurately.

(Vasudevan, 2018) contributed an in-depth investigation of cracking in PMMA, dedicating a chapter of his PhD manuscript to the transition phase from dynamic to quasi-static propagations. During the experiments, load cell and clip gauge have been used to obtain force and displacement data, respectively. Crack tip positions have been obtained by using a high-speed camera system (temporal and spatial resolution of 48 kfps and $\sim$ 175 kpix, respectively) and a home-made algorithm. By combining these results, SIF and thereby fracture energies have been derived through a numerical (FE) based compliance chart relying on load and displacement data. However, difficulties in this setup arise in the high-velocity regime, where the accuracy for load and displacement measurements can not be assured. Furthermore, the chosen sample geometry had the unique purpose of studying dynamic to quasi-static crack propagation transitions. TDCB specimens with the notch being blunted by a circular hole allow for the initiation of a dynamically propagating crack while using low tensile extension rates ($\sim 2.5\,\mu$m.s^{-1}). Here, with respect to the theoretical concept of fracture in PMMA (Figure 1), the crack finds its way back to the master curve far below the value of v_a by following the path D$\longrightarrow$A, which can be explained by the relatively low extension rate. After the arrival of the initiated dynamic crack, by assuming an infinite sample length, the crack would have propagated entirely quasi-static in the wake. Hence, the presented experiments are a matter of quasi-static experiments introduced by dynamic crack propagation.

Under the scope of providing a model of the fracturing behavior in PMMA, (Vincent-Dospital et al., 2020) performed wedge-splitting fracture experiments on PMMA samples over a wide range of quasi-static driving speeds (1.6 μm.s^{-1} to 1.2 mm.s^{-1}). Force data were monitored in real-time by the load cell, while the propagating crack was followed by a high-resolution camera. In this case, for quasi-static propagation measurements, the temporal resolution of 10 fps provided crack length and subsequently velocity measurements by post-treating the images with the in-house crack tip detection algorithm. On the other hand, fast crack propagations were detected, through an oscilloscope, by the successive rupture of parallel 500 μm large chromium or gold lines on the surface. Numerical charts based on FE analysis supported the determination of mode I related stress intensity factor K_I. Energy release rates then were retrieved under plane stress assumption.

In summary, literature shows that the investigation of region II has been conducted by experimental procedures only suitable for either of the two other enclosing regions. Crack-speeds are usually obtained from camera systems (either high-speed or high-resolution) and tracking algorithms. K_I and subsequently energy release rates are

mostly obtained from numerical compliance methods or analytical charts, which are limited due to low accuracies in high loading rate cases. Note that region II is classically referred to as 'forbidden' velocity regime, but the model proposed in (Vincent-Dospital et al., 2020) suggest that it could be reached if the simulation or the experiment can be conducted by controlling the crack speeds. However, this is impossible to achieve neither numerically nor experimentally, with the energy release rate being governed by the applied load as the controlled parameter. Beyond the methodological contribution of investigating alternate cracking through high-speed DIC, we address in the following the experimental investigation of alternate cracking by focusing systematically on crack velocities, SIFs and their relation to the fracture surface. Like this, transitions from dynamic to quasi-static and quasi-static to dynamic can be studied. Hence, we propose a compromised experimental configuration, based on high-speed fullfield measurements (DIC), and on asymptotic solutions of kinematic fields to get not only FE independent and chart-free estimations of the SIFs, but also sub-pixel estimations of crack tip positions. Additionally, the contribution of this study can be summed by the attempt of providing experimental data for an improved estimation of the hysteretic fracturing behavior described by the loop following path B, C, D and A' in Figure 1.

3 Experimental program

Experiments have been performed during two independent experimental campaigns, called M1 and M2. Setup, material and loading conditions have been kept consistent, while using different sample thicknesses. 5 mm and 8 mm thick plates have been used for the specimen preparation of the M1 and M2 campaign, respectively.

3.1 Material and geometry of the specimen

In this study, alternate cracking, specific to Poly(methyl methacrylate) (PMMA) (Ravi-Chandar and Yang, 1997), as well as polyesters (Leevers, 1986), epoxy resins (Yamini and Young, 1977), rubber (Isherwood and Williams, 1978) and polymeric adhesives (Maugis and Barquins, 1988), is investigated. Due to its ideal brittle behavior and the presence of different cracking behaviors at varying loading conditions, PMMA is a material of great interest in fracture mechanics research and an ideal model material for this investigation. Here, molded PMMA (Perspex® and Plexiglas® for M1 and M2 campaign, respectively) was the material of choice. For details on material properties and its mechanical behavior, the authors refer to (Ali et al., 2015). The tapered double-cantilever beam (TDCB) shape was chosen to have a constant specimen compliance w.r.t. the crack length and ensure stable crack propagation. The samples were obtained by using a class 4 laser cutting machine (130 W). Notice that pin holes have been manually drilled to avoid laser beam (conical shape) related clearance angles (~1.5°), which would induce transverse load, i.e. potential sample bending. The detailed sample geometry can be found in Figure 3.

Notice that caution is required regarding sample preparation for achieving good repeatability. Indeed, PMMA fracture behavior is very sensitive to temperature (Atkins et al., 1975a,b), but also to any significant interaction with organic solvents (Wang et al., 1994). In that context, ethanol (eventually used for surface cleaning) should be avoided, and solvent free paints should be preferred for DIC patterning of the sample surface.

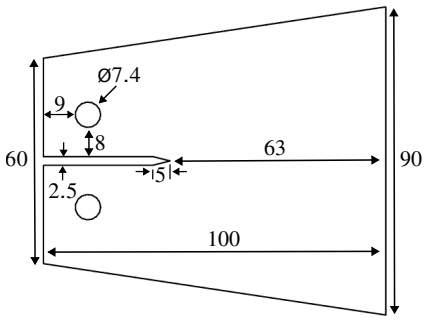

Fig. 3: Sample geometry [mm].

Table 1: Second loading stage extension rates applied during the experiments.

Extension rate [mm.s^{-1}]	Test
1.0	M1-T2, M2-T15, M2-T19
0.5	M1-T3, M1-T6

3.2 Loading and test configuration

All experiments were performed using an Instron all electric dynamic and fatigue testing system (ElectroPuls E10000) with a load cell of 1 kN maximum loading capacity in a temperature controlled (21 °C) room. Beforehand, preliminary experiments were conducted to identify the alternate cracking domain within the experimental environment. With respect to the used material and geometry, solely quasi-static propagation has consistently been found below extension rates of 0.1 mm.s^{-1}. First dynamic bursts have been observed between 0.1 mm.s^{-1} and 0.5 mm.s^{-1} with strong variability from one test to another. Following this domain of inconsistency, alternate cracking was systematically determined in a repeatable manner (Figure 2). Entirely dynamic cracks have been found for extension rates above 20 mm.s^{-1}. Extension rates close to the lower end of the identified alternate cracking domain have been used to provoke higher repetition of crack arrests while maintaining reasonable quasi-static lengths. Additionally, to achieve an experimental consistency of the crack line by avoiding influences of the notch tip on the subsequent cracking and the point of initiation for different cracking experiments, a two stages loading procedure was established:

1. *Controlled quasi-static crack propagation.* During this stage a relatively slow extension rate of 0.01 mm.s^{-1} was imposed. Stage change has been executed by the help of the Static Break Detector option within the Instron WaveMatrix software (Figure 4). The tool is designed to trigger a user-selected action when the monitored signal falls below or rises above a pre-defined value (event value). 25 N was selected for the event value, which generally led to slow propagating cracks of about 5-10 mm.
2. *Alternate crack propagation.* A second loading stage was introduced to release the alternate crack propagation from this fresh pre-crack. During this stage, the extension rates being used during the different experiments are shown in Table 1.

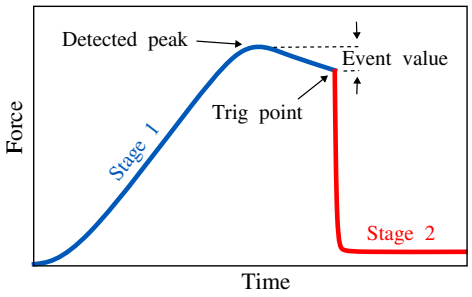

Fig. 4: Example of stage change method (Static Crack Detection).

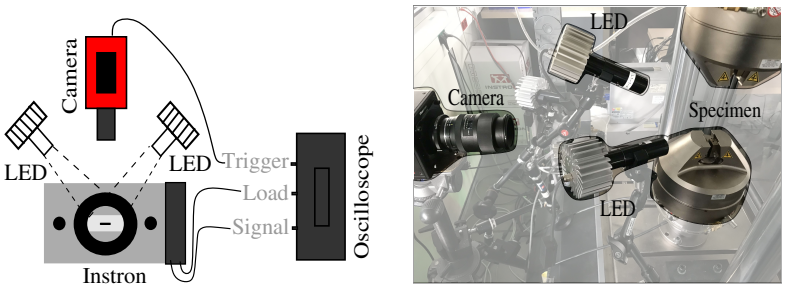

(a) (b)

Fig. 5: Experimental setup: (a) sketch, (b) picture.

3.3 Experimental setup

Alternate cracking is a phenomenon, where two entirely different cracking behaviors are to be found during solely one fracturing process. Hence, for relevant data acquisition during the dynamic crack propagation phases, the experiments are in need of high speed imaging. Here, images of the cracking sample were captured using a Photron FASTCAM Mini AX camera system with an acquisition speed of 40 kfps. Sufficient lighting of the sample was ensured by LED projectors (EFFI-Sharp PWR FF by Effilux). Master device for camera triggering has been the tensile machine, which sent a 5 V TTL trigger signal to an oscilloscope once the second loading stage has been activated. A threshold in the oscilloscope was then used to trigger the camera system. Hence, only second loading stage results have been recorded. Picture and sketch of the experimental setup can be seen in Figure 5. Camera specifications related to the experiments are presented in Table 2.

3.4 Fracture parameters by DIC

The foundation for retrieving the sought-after fracture mechanics variables is found in DIC by providing full-field displacement measurements from sequential images. By following the principle of conservation of brightness between a reference (f) and a deformed image (g), i.e. the equation of optical flow, DIC presents an ill-posed non-linear

Table 2: DIC hardware parameters

Campaign	M1	M2
Camera	Photron FASTCAM Mini AX	
Image resolution	896×160 pix	
Acquisition rate	40,000 fps	
Exposure time	25 μs	
Lens	TOKINA 100 mm	
Aperture	f/2.8	
Field of view	74×13 mm	64.5×11.5 mm
Image scale	1 pix = 83 μm	1 pix = 72 μm
Patterning technique	Spray paint	

inverse problem:

$$f(\underline{X}) = g(\underline{X} + \underline{u}(\underline{X})) \tag{1}$$

with $\underline{u}(\underline{X})$ being the sought displacement field. To bypass this ill-posed problem, the pixel displacement has to be parameterized using shape functions. Here, FE discretization has been used (Besnard et al., 2006). Eventually, the problem can be linearized and solved iteratively in a least-squares sense. A median regularization is used to mitigate detrimental impact of noise and smaller elements. By post-treating the displacement field, variables relevant for fracture mechanics analysis (e.g. SIFs and crack tip positions) were derived through Williams' series expansion. Traditionally, in the case of a semi infinite linear elastic isotropic media, stress and displacement fields around the crack tip depend on SIF, the distance to the crack tip (r) and the angle (θ) in a polar reference system attached to the crack tip (Williams, 1957). Thus, by knowing the displacement field through DIC and projecting it onto the analytical solution, different fracture mechanics parameters can be derived through a non-linear inverse problem (Roux and Hild, 2006; Réthoré, 2015; Roux-Langlois et al., 2015). The displacement field around the crack tip is written as following:

$$u(r,\theta) = \sum_{i=I,II} \sum_{n=-\infty}^{\infty} A_i^n r^{n/2} g_i^n(\theta) \tag{2}$$

with the distance to the crack tip r, the angle θ in a polar reference system attached to the crack tip, Williams' coefficients A and base function g. The base function $g_i^n(\theta)$ has the following form:

$$g_I^n(\theta) = \frac{1}{2\mu}\begin{bmatrix}(\kappa + n/2 + (-1)^n)cos[(n/2)\theta] - (n/2)cos[(n/2-2)\theta] \\ (\kappa - n/2 - (-1)^n)sin[(n/2)\theta] + (n/2)sin[(n/2-2)\theta]\end{bmatrix}_{(e_t,e_n)} \tag{3}$$

$$g_{II}^n(\theta) = \frac{1}{2\mu}\begin{bmatrix}-(\kappa + n/2 - (-1)^n)sin[(n/2)\theta] + (n/2)sin[(n/2-2)\theta] \\ (\kappa - n/2 - (-1)^n)cos[(n/2)\theta] + (n/2)cos[(n/2-2)\theta]\end{bmatrix}_{(e_t,e_n)} \tag{4}$$

with μ and κ being the shear modulus and the Kolossov's constant, respectively. Kolossov's constant under plane stress is $\kappa = (3-\nu)/(1+\nu)$ with ν being the Poisson's ratio.

Equation 2 states, that displacements can be computed for an infinite sum of modes. However, limiting the solution to n_{min} = -3 and n_{max} = 7 is sufficient to retain the relevant crack features. For quasi-brittle medium, good agreement of the mechanical fields can be established outside the process zone of the crack for the following Williams' series coefficient (A_i^n) solutions:

Table 3: DIC & Williams' series parameters

Campaign	M1	M2
Test	2, 3, 6	15, 19
DIC		
Software	UFreckles (Réthoré, 2018)	
Discretization	FE-based global DIC	
Shape function	Bi-linear quadrilateral Lagrange element (Q4P1)	
Element (subset) size	0.581 mm (7 pix)	0.576 mm (8 pix)
Post-filtering	Median filter using 1^{st} neighbours applied to U	
Williams' series projection		
E	3.5 GPa	
ν	0.32	
R_{min}	1.16 mm	1.15 mm
R_{max}	6.39 mm	6.34 mm

n = 0, in-plane rigid body translations
n = 1, asymptotic terms K_I and K_{II}
n = 2, T-stress and in-plane body rotations

Notice that the projection zone is defined by R_{min} and R_{max}. On the one hand, the asymptotic behaviour near the crack tip of the fields computed by the super-singular terms (n <0) do not provide any physical meaning and are therefore classically neglected. However, when the crack tip position is sought, these super-singular functions appear in the required basis (n=-1 being, up to a scaling factor, the derivative of n=1 with respect to the assumed crack tip position). To not induce biases due to truncation, terms for n down to -3 are considered. Hence, data at a distance to the crack tip smaller than R_{min} are discarded to maintain reasonable conditioning of the least-squares problem. On the other hand, R_{max} – defining the projection zone size externally – has to be small enough to avoid influences of the free boundary, but large enough to still include a sufficient amount of mesh points in the domain. The right size of projection zone, i.e. defining R_{min} and R_{max} (see Table 3), has been identified through a parametric study. Furthermore, by using a pre-defined crack path, the super-singular term n = -1 is used to estimate the position to the equivalent elastic crack tip along this path (Réthoré et al., 2011). In the context of the study, relevant coefficients of the solution imply n = -1 and $n = 1$, i.e. crack tip detection and SIFs. It is worthwhile mentioning, that the quasi-static form (not in function of the velocity) of the displacement field around the crack tip is used in line with previous works showing that marginal errors can be assumed for velocities below $0.5c_R$ (Lee et al., 2010). Eventually, the outcome is used to derive crack velocities and energy release rates. The second, under the assumption of plane stress, has been computed through Equation 5.

$$G = {K_1}^2/E \tag{5}$$

with K_1 and E being the SIF related to mode I and Young's Modulus, respectively. DIC and Williams' series projection results have been obtained entirely by accessing the library of the open-source software UFreckles (Réthoré, 2018). All relevant parameters for the two procedures are listed in Table 3.

3.5 Post-processing and method synchronization

To get derivatives such as the crack velocity, raw crack tip measurements had to be filtered accordingly. The need for high speed imaging to obtain sufficient amount of data points during dynamic crack propagation led to comparable huge sets of data for the quasi-static propagation phases. With a difference of tens (dynamic) to thousands (quasi-static) of data points between the two regimes, the data set had to be separated and post-filtered by different kernel sizes. The post-filtering has been performed by using a Savitzky Golay filter with a second order polynomial. Depending on the regime affiliation, a filtering window size of 7.275 ms (291 frames) or 75 μs (3 frames) has been applied for quasi-static and dynamic regimes, respectively. The relatively strong and rather insignificant kernel size for, respectively, the quasi-static and dynamic phases deemed to be fitting to not drastically influence crack speed evolution in the quasi-static parts or decrease the accuracy of the dynamic phase measurements.

To investigate crack kinetics, not only high-speed recordings but also post-mortem high resolution microscopy was performed. Therefore, the comparison of data obtained by techniques with different spatial resolutions are in need of harmonization. Here, as the notch tip can easily be identified in DIC and microscopic images, it served as common point of reference. By doing so, DIC obtained crack tip positions were tied to post-mortem microscopic images. The most dominant error sources related to the process of spatial matching are the manual selection of the notch position (σ_{notch}) and the pixel to meter conversion ('pix2m') uncertainty (σ_{pix2m}). Due to camera resolution, used lens and clearance angle of the sample cut, the uncertainty on the notch tip localization has been evaluated to be about $\sigma_{notch} = 1.5$ pix. Pixel to meter conversion values have been identified by analysing ruler images taken before each test, with the help of the Fast Fourier transform (FFT) approach. The uncertainty of the 'pix2m' value has been evaluated to be about $\sigma_{pix2m} = 1.12 \times 10^{-3}$ pix as the FFT sampling was chosen to be the horizontal pixel size of the image (896 pix). First approximation of the crack tip localization uncertainty ($\sigma_T(a)$) can be evaluated through the following equation:

$$\sigma_T(a) = \left(a \times \sigma_{pix2m} + \sigma_{notch}\right) \times pix2m \tag{6}$$

with a being the crack length at any position of interest. A maximal error of approx. 160 μm and 140 μm have to be expected for the considered field of view (FOV) for experiments related to campaign M1 and M2, respectively.

4 Results

PMMA samples were subjected to the above described loading condition (see Chapter 3.2) and followed by a high-speed camera system. About 40,000 successive images over a duration of one second were obtained for each experiment. The images were used for DIC analysis and subsequently for the retrieving of fracture mechanic parameters. Five tests have been taken into consideration coming from two different experimental campaigns (M1 and M2). Representative for all experiments, full-field displacement measurements (in y-direction) for the first and last recorded frame superimposed on the appropriate image of experiment M2-T15 are presented in Figure 6(a) and Figure 6(b), respectively. In the same configuration, corresponding Williams' series projection areas are presented in Figure 6(c) and Figure 6(d). Crack length data, retrieved through the process of Williams' series expansion, are then presented in Figure 7 in the form

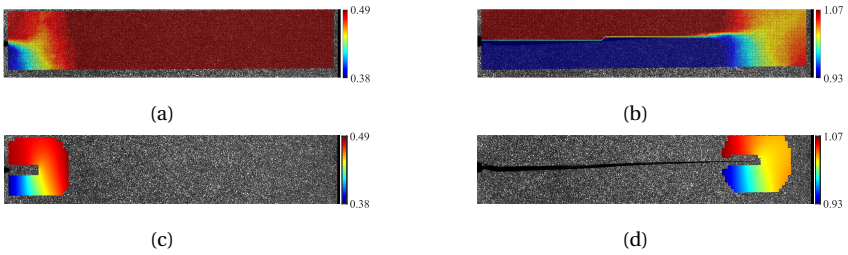

Fig. 6: Entire displacement field in y-direction [mm] and its corresponding Williams' series projection [mm] on the process zone surrounding the crack-tip (defined by R_{min} and R_{max}) of the first ((a) and (c)) and last recorded image ((b) and (d)) for experiment M2-T15. The used Williams' series parameters are listed in Table 3.

of the temporal evolution of the normalized crack length. This is defined by the crack length relative to the length of the samples (63mm from notch tip to sample boundary). Furthermore, stable first stage crack propagations have been taken into consideration for the presentation of the normalized crack length. This causes each experiment to start from its own individual pre-crack length.

Each crack length evolution is showing a similar global behavior. After the pre-crack, almost horizontal lines describe the first quasi-static propagation of the crack. Following vertical jumps indicate the dynamic cracking. The combination of the two regimes is what is referred to as alternate cracking of the sample. This is depicted by the repeating occurrence of vertical jumps surrounded by quasi-static phases. 4, 3, 2, 2 and 2 vertical lines, i.e. dynamically propagating cracks, are observed for tests M1-T2, M1-T3, M1-T6, M2-T15 and M2-T19, respectively. The frame rate chosen for this investigation leads to dynamic crack propagation phases being sampled by 4 to 7 images depending on their propagation length. It will allow to have good estimations of the mean velocity, while not being sufficient to accurately probe potential speed variations. Oscillations in the crack length of the quasi-static rest phases appear always closely following the dynamic bursts. These fluctuations can be explained by system vibrations due to history-dependent effects induced by brutal, instantaneous dynamic bursts. It leads to oscillations of the crack lips (opening and closing) causing the crack tip detection to record backwards moving cracks. Furthermore, as they become more prominent when the crack approaches the free end of the sample, the vanishing resistivity of the entire sample seems to have an enhancing effect on the phenomenon.

For sake of clarity, two experiments will be prioritized for the continuation of the discussion. For this, M1-T2 and M2-T15 have been selected as representatives of the two experimental campaigns as the tests with the most quasi-static rest repetitions within their experimental campaign.

4.1 Velocities

To further differentiate among the crack propagation types observed during alternate cracking, crack speeds have been derived from the crack length. Figure 8 is showing the spatial evolution (as a function of crack length) of the crack speed for experiments M1-T2 and M2-T15. Only effective crack tip positions, i.e. always keeping the most ad-

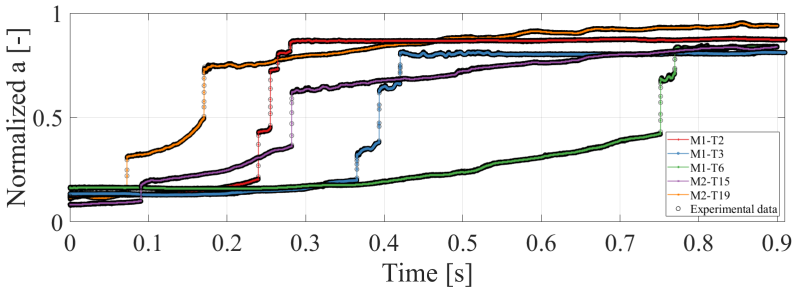

Fig. 7: Normalized crack length (1.0 = 63 mm) as a function of recording time [s] for all five experiments.

vanced position as real position of the crack tip, have been taken into consideration to avoid the influences of crack length oscillations discussed before. Two strongly different crack speeds are observed in the experiments. Variations in dynamic crack speeds are rather small, while crack speeds associated to quasi-static propagation show significant oscillatory behavior. By taking both experiment M1-T2 and M2-T15 into consideration (Figure 8), average crack tip speeds up to 10.5 cm.s^{-1} and between 14 m.s^{-1} to 107 m.s^{-1} are observed during quasi-static and dynamic crack propagations, respectively. Average dynamic crack speeds around ∼14 m.s^{-1} would portray a divergent observation from the literature (Hattali et al., 2012; Vasudevan, 2018) documented dynamic crack speed measurements during similar experiments. However, by taking the fracture surface into consideration, one can see tiny rest bands (see Figure 9) appearing within the flat parts of some dynamic bursts. The specific surface pattern is regularly found during transition from dynamic to quasi-static phases (see Detail 2 and Detail 3 in Figure 9). Thus, the rest bands suggest small pauses of the crack, too short to be visible in the recordings (interframe of 25 μs) but long enough to significantly influence the crack speed measurements during these dynamic phases considering the frame rate of 40 kfps. The appearance of rest bands can be interpreted as intermittent behavior of dynamic cracks. The amount of rest band appearances during the different dynamic bursts for all considered experiments are listed in Table 4. Associated to this Table, Figure 10 provides a relation between crack speeds and their corresponding propagating length. Here, cracking phases with biased velocity measurements are marked in red. Globally, two groups of propagation phases can be observed in the figure. Cracks with rest bands fall all within the lower velocity range, while the others are found above. It appears that the limit average velocity separating these two can be allocated at approx. 60 m.s^{-1}. Indeed, with sufficient temporal resolution to capture velocity variations during dynamic propagation, rest band deceleration's could have been singled out. This would most certainly cause the upwards shift in average velocity during these phases with the option of excluding rest bands. However, by taking all bursts into consideration, a relation of increasing average velocity with increasing burst length can be assumed. A specific case is found during the first dynamic burst of M2-T15. The particular surface roughening is observed, even though no rest band is entirely formed. Nevertheless, crack deceleration influencing the velocity measurement have to be expected. Thus, this burst will be considered as biased and included to the rest band effected bursts. With an average velocity of ∼60 m.s^{-1}, the dynamic burst seems to be at the velocity threshold for the formation

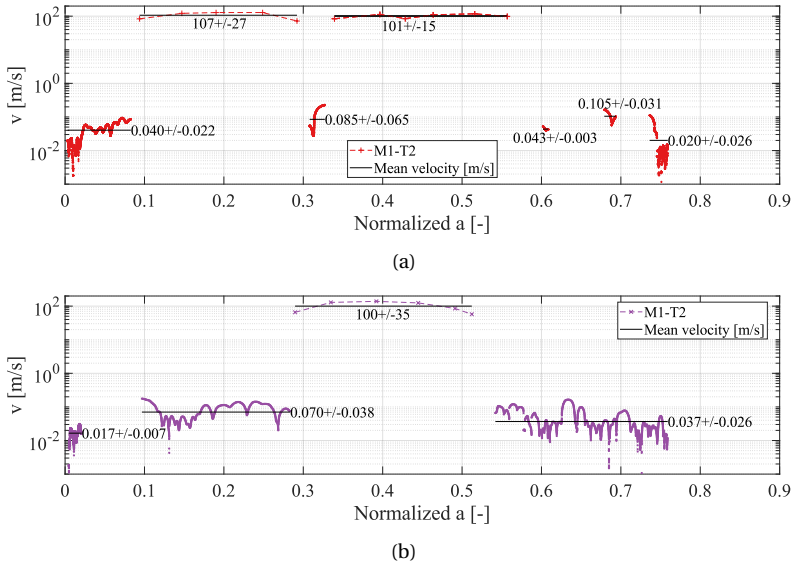

Fig. 8: Crack tip speed (v) [m.s^{-1}] as a function of the normalized crack length (a) [mm]. Black bars present the phase-dependent mean velocity [m.s^{-1}], while their value is presented as numbers next to the bar with its standard deviation (std).

of rest bands. Hence, if dynamic bursts affected by rest bands (biased velocity measurements) are neglected, a 'forbidden' velocity regime of ∼36 cm.s^{-1} to ∼36 m.s^{-1} can be implied taking all conducted experiments into consideration. This is expressed in Figure 11, showing velocities with respect to the normalized crack length for all conducted experiments excluding dynamic phases that are considered to be biased. Notice, with average velocities above the identified threshold value (∼60 m.s^{-1}) for the formation of rest bands, instantaneous velocity measurements at the beginning and the end of rest band free dynamic burst can fall below the threshold and thereby present the upper bound of the 'forbidden' velocity regime.

4.2 Connections to the fracture surface

In the following, more attention is given to the relation of experimental data and fracture surfaces. Microscopic images have been obtained by an optical microscope (Nikon) with a resolution of 0.67 μm.pix^{-1}. K_I and velocity data as a function of the crack length are presented in face with their corresponding fracture surface in Figure 12. Here, only the propagation parts between notch tip and the beginning of the second dynamic phase are presented. Like this, two quasi-static to dynamic and one dynamic to quasi-static transition can be seen. Crack propagation is from left to right and marked in the left bottom corner of the figures. DIC (K_I, v) and microscopic observations (fracture surface) have been spatially matched with respect to the notch tip. Fracture surfaces were recreated by manually stitching microscopic images with a field of view of 1.715 × 1.286 mm. Hence, minor light differences can be seen between the sub-frames.

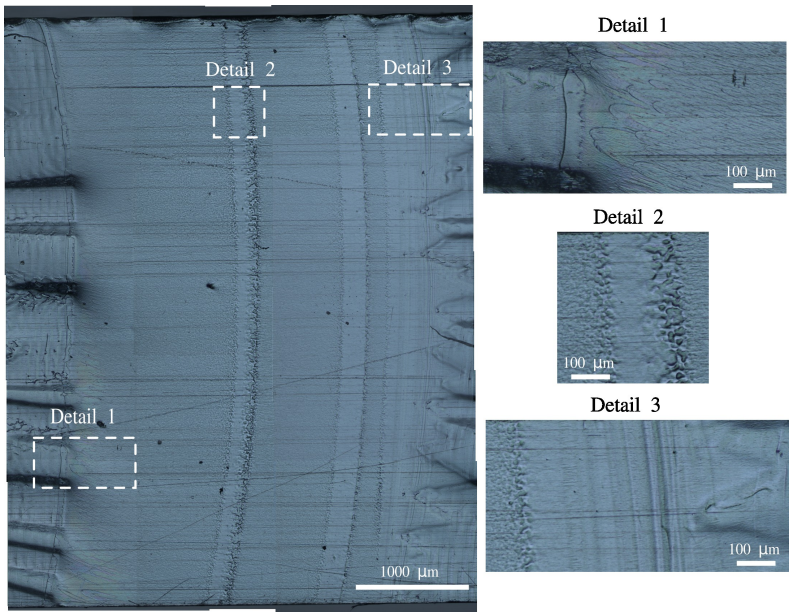

Fig. 9: Example fracture surface showing different particular surface observations. Detail 1, 2 and 3 are showing nucleation phase, rest band and the dynamic to quasi-static deceleration phase with the appearance of Wallner lines, respectively.

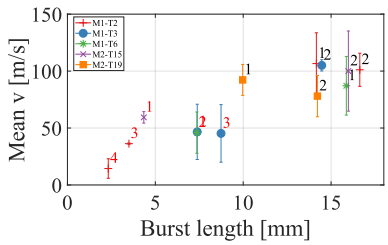

Fig. 10: Mean velocity [m.s^{-1}] as a function of the burst length [mm] for the dynamic phases of all conducted experiments. The chronological order of the different dynamic burst for each individual test is given by the numbers next to the data points. Red colored numbers indicate the appearance of at least one rest-band during this particular dynamic burst, while the error bars give the variation (std) of the velocities for each dynamic phase.

Test	DYN-burst			
	1	2	3	4
M1-T2	0	0	2	2
M1-T3	1	0	3	-
M1-T6	0	2	-	-
M2-T15	1*	0	-	-
M2-T19	0	0	-	-

Table 4: Amount of rest band appearances during the dynamic bursts. (*) means specific roughening of the surface observed, which implies the early formation of a rest band that is yet not fully evolved. However, biased velocity measurements still have to be expected.

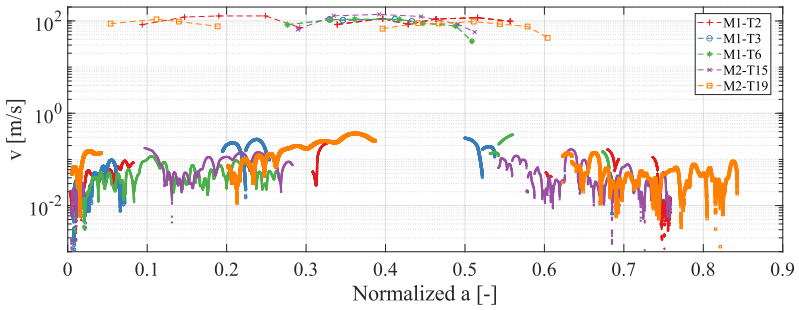

Fig. 11: Velocity [m.s^{-1}] as a function of the normalized crack length [mm] for all conducted experiments.

The most striking observation is the regime and phenomenon-dependent fracture surface pattern: quasi-static and dynamic fracture processes produce wave-like and flat surface patterns, respectively. Macroscopically, the two entirely different mechanisms therefore produce different fracture surfaces. Differences in fracture surface with respect to the experiments coming from the two campaigns are found in height of the wave-like ligaments and the curvature of the crack fronts. Crack front curvatures arise by focusing on the transitions between the two phases. Furthermore, the particular roughening of the fracture surface between 8 to 10 mm in M2-T15 (12(b)) is indicating the partial formation of a rest band, which has been discussed before. Other particular observations are the specific rough pattern appearing during transition from dynamic to quasi-static with Wallner lines (Wallner, H., 1939; Bonamy and Ravi-Chandar, 2003) (Detail 3 in Figure 9) and the occurrence of conical marks related to micro-crack formations ahead of the main crack during the quasi-static to dynamic transition phases (Detail 1 in Figure 9) (Ravi-Chandar and Balzano, 1988). These conical surface marks are only found in the really beginning of the dynamic bursts suggesting, from (Guerra et al., 2012), crack speeds above ∼165 m.s^{-1}. Highest velocities can thereby be expected in the beginning of dynamic bursts. K_I and velocity measurements underline this dependency. With severe differences (around two orders of magnitude) in velocities separating the two types of crack propagation, K_I is globally showing a decrease as the crack propagates dynamically and a recovering increase as it rests during the quasi-static phases. As longer lasting quasi-static propagations are present (see Figure 12(b)), K_I and v find itself oscillating around a constant value.

Special interest is given in the following to the transition phase dynamic to quasi-static propagation related to the first quasi-static rest of the two experiments. During the quasi-static rest of the M1-T2 experiment (Figure 12 (a)), K_I consists out of two phases: Increasing from ~ 0.9 MPa$\sqrt{m}$ to ~ 1.2 MPa$\sqrt{m}$ (~ 27 mm to ~ 27.6 mm), while stabilizing around ~ 1.2 MPa$\sqrt{m}$ (~ 27.6 mm to ~ 28.4 mm) before the occurrence of the following dynamic burst. By relating these observations to the measured velocities, one can notice a drop in crack tip speed when K_I has a sudden change and an overall decrease of crack speed during this first phase. During the second stable K_I phase, the velocity increasingly converges towards a stable crack tip speed before the sudden jump into the dynamic region. Linking the observations to the fracture surface, the formation of triangular surface patterns (see Detail 3 in Figure 9 for zoomed view on an

example surface) seems to be related to the first phase, while the stable second phase can be linked to the continuation of the newly formed wavy fracture pattern. Overall, similar trends are found in the quasi-static rest obtained from the M2-T15 experiments (Figure 12 (b)). K_I increases with decreasing crack speeds during the formation of the triangular crack pattern, while both stabilize in the continuation of the wavy pattern. In detail, K_I values increase during the first phase from ~ 1.1 MPa$\sqrt{m}$ to ~ 1.4 MPa$\sqrt{m}$ (~ 16 mm to ~ 15 mm), while decreasing again until 22 mm to around ~ 1.3 MPa$\sqrt{m}$ with stronger oscillations. However, until ~ 22.5 mm, a sudden increase back to 1.4 MPa$\sqrt{m}$ is observed, followed by a phase of continuity before the crack starts to propagate dynamically again at ~ 23.7 mm.

When focusing on the fracture surface at the beginning of the quasi-static phase, both specimens show the particular roughening and the appearance of Wallner lines. According to velocity measurements, this area seems to be the result of an intense deceleration zone. Here, a variable e is used to depict the distance of the end of this particular rough pattern and the first appearance of a Wallner line. A relationship of this distance e (Figure 13(b)) with the mean crack tip speed of the preceding dynamic phase is established in Figure 13(a) for the quasi-static rests of all conducted experiments. Red color numbers again indicate the presence of rest bands falsifying the velocity measurement of this particular dynamic burst. Hence, if dynamic bursts with rest band occurrences are neglected, a trend with a growing relationship of dynamic velocity and distance e can be suggested. While first Wallner lines seem to appear after 193±78 μm for mean dynamic crack speeds of 85±5 m.s^{-1}, they first appear after 490±125 μm for mean crack tip speeds above 100 m.s^{-1}. It seems to show that depending on the velocity, a critical distance is required (with almost linear trend) to reach quasi-static propagations.

4.3 Energy release rate

Energy release rates have been computed from K_I to reproduce the kinetic law of materials showing alternate cracking (Section 2.1). Again, a detailed presentation of the hysteresis will only be presented for two tests (here, M1-T2 and M2-T19). For clearer visualization, only the crack propagation phases directly associated with the alternate cracking are presented. This means, only the phases surrounded by dynamic bursts are taken into consideration with the hysteresis always starting with the first dynamic burst. In each of the two sub figures, presented in Figure 14, two related graphs are found: the temporal evolution of the crack length ($a(t)$) and the energy release rate as a function of the crack tip speed ($G(v)$). Each individual phase of cracking is colored concordant over the two plots. Also, triangular and square markers indicate the beginning or the end of a phase, respectively.

Let us first look at test M1-T2 (Figure 14(a)). The hysteretic behavior of the fracturing is here introduced by a first dynamic burst (light blue) following the theoretical corner points C to D. During this propagation phase, the energy release rate drops from $\sim$520 J.m^{-2} to $\sim$195 J.m^{-2}, while the crack speed undergoes an increasing, stabilizing and decreasing phase with velocities around 85 m.s^{-1}, 120 m.s^{-1} and 70 m.s^{-1}, respectively. Subsequently, no data points are acquired until the first points in the quasi-static region, indicating the first jump between the two accessible regions. By arriving at the first quasi-static propagation phase (dark blue), G rises from $\sim$240 J.m^{-2} to $\sim$375 J.m^{-2}, while the crack speed continues to decrease from 5 cm.s^{-1} to 3 cm.s^{-1}. After this, while G continues to grow ($\sim$375 J.m^{-2} to $\sim$420 J.m^{-2}), v finds itself increasing from the low

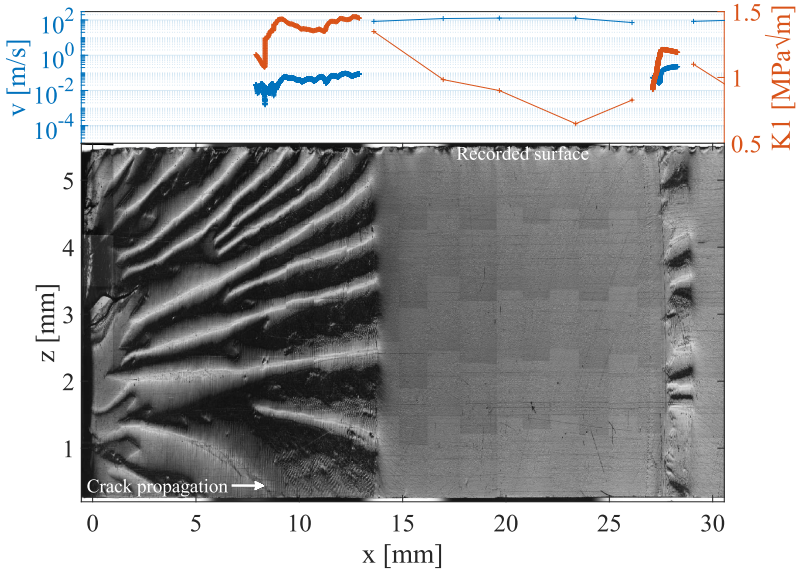

(a)

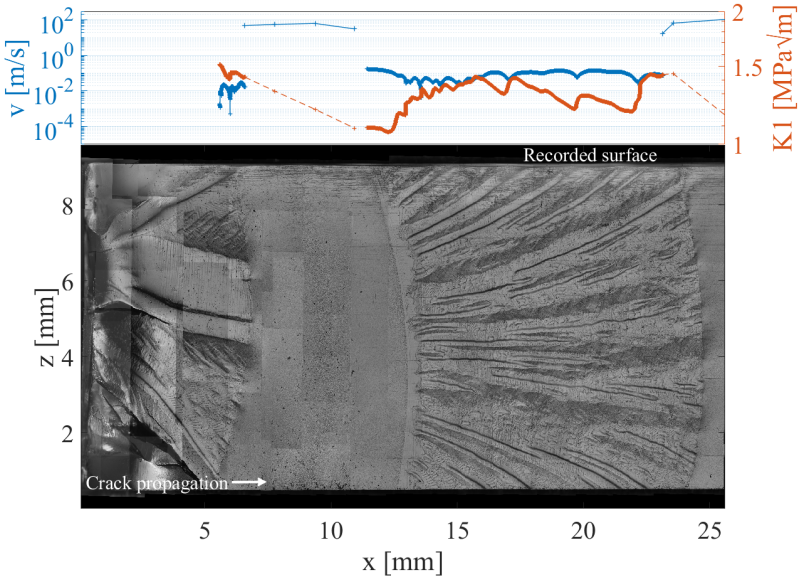

(b)

Fig. 12: Velocity [m.s^{-1}] and K_I [MPa$\sqrt{m}$] as a function of crack length [mm] in face with the microscopic image of the fracture surface for the experiments: (a) M1-T2 and (b) M2-T15. A spatial matching error between DIC and microscope measurements of ~160 μm and ~140 μm has to be considered for M1-T2 and M2-T15, respectively.

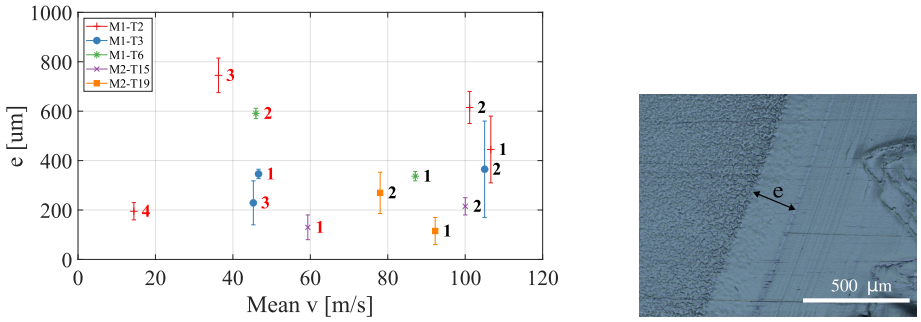

(a) (b)

Fig. 13: (a) Mean velocity during dynamic crack propagation [m.s^{-1}] as a function of e-length (i.e. distance from dynamic micro roughening to Wallner lines) [μm] of the subsequent DYN to QS transition phase for all experiments. Error bars present the measurements on the two free edges of the fracture surface over the sample thickness. The chronological order of the different dynamic burst for each individual test is given by the numbers next to the data. Red colored numbers indicate the appearance of at least one rest-band during this particular dynamic burst. (b) Example of the measured distance e on the fracture surface.

point to around 15 cm.s^{-1}. With G decreasing after reaching its peak value (~420 J.m^{-2}), the crack continues to accelerate to 23 cm.s^{-1} before jumping back to the dynamic region. Globally, this repeats itself until full crack arrest. However, the last two dynamic branches (orange and light red) have to be taken with caution since the measurements are influenced by the presence of rest bands. Furthermore, the seemingly separation of the last quasi-static phase (dark red) into two arms can be explained by the post-treatment done on the crack length to remove post-dynamic oscillation leading to zero velocities for a short duration. Additionally, it is worthwhile mentioning that the value of critical fracture energy (G), introducing the 'forbidden' region II, is 430±30 J.m^{-2} for all quasi-static phases. Test M2-T19 (Figure 14(b)) generally follows this description with the difference of a long quasi-static rest resulting in more data points and stronger velocity oscillations during this phase.

To conclude the results of this study, all experimental data (excluding phases with biased velocity measurements) is presented in the same (v,G) space (Figure 15). Additionally, an entirely quasi-static experiment, that has been subjected to an extension rate (0.07 mm.s^{-1}) close to the threshold of the observed appearance of alternate cracking, was added. To place the experimental results into the context of the literature, experimental data points from (Vincent-Dospital et al., 2020) and (Scheibert et al., 2010) (quantitatively extracted using online software (Rohatgi, 2022)) were furthermore included. While our entirely quasi-static experiment seems to align well with the quasi-static experiments conducted in (Vincent-Dospital et al., 2020), alternate cracking results do seem to add the missing experimental data to adequately cover the transition between quasi-static and dynamic crack propagation in the full spectrum of PMMA fracturing. Starting with the dynamic branch, experimental data points found in this study fit well the trend of existing literature. However, the last value of G (before jumping to the quasi-static phase) is systematically found below any G value of the quasi-

static regime, and therefore below the expected value of G_c. In detail, velocity measurements and energy release rates introducing the jump from dynamic to quasi-static propagation are found to be 236±40 J.m^{-2} and 67±31 m.s^{-1}, respectively. During quasi-static phases, with velocities reaching a function of the macroscopic loading rate after the decelerating phase, the crack grows at almost constant speed. Observed variations during quasi-static propagation can be explained partly by physical and partly by post-dynamic effects. Avalanche values for energy release rate and velocity marking the beginning of the 'forbidden' region II are found to be 497±92 J.m^{-2} and 0.19±0.15 m.s^{-1}, respectively. Taking both sides into consideration, region II, i.e. 'forbidden' velocity regime, is thereby found to be more narrow than presented in literature. Nevertheless, a brutal switch is seen from the rate dependent dynamic branch to the quasi-static regime with only, as transition, the deceleration distance e.

General variations in the energy release rate are found to be in line with the literature. In the quasi-static regime, the material strength increases with increasing strain rates due to the viscosity of PMMA. The resulting increase of G in the quasi-static regime is supported by the experimental data of Vincent-Dospital et al. (Vincent-Dospital et al., 2020). The increase in the energy release rate in the dynamic regime can be explained by the increase of the process zone around the crack tip, which is in line with Kanninen's theory (Kanninen and Popelar, 1985). However, differing energy release rates for dynamic crack initiation and arrest – where the SIF at dynamic crack initiation $K1D_{ini}$ has been found to be higher than at dynamic crack arrest $K1D_a$ – have also been discussed in Grégoire et al. (Grégoire et al., 2009). Furthermore, influences on the fracture surface of the variations of the dynamic crack propagation and the increase of surface roughness due to the appearance of micro-cracking have also been discussed in the literature (Ravi-Chandar and Balzano, 1988; Grégoire, 2008; Dalmas et al., 2013). This is in line with the presented observations, where conical shapes on the fracture surface (micro-cracking) are found at the beginning of the dynamic propagation (Figure 9, detail 1) with high levels of G. At the same time, they vanish as G decreases to the point of dynamic crack propagation arrest.

5 Conclusions and perspectives

For this study, alternate cracking in PMMA has been observed by high-speed imaging and investigated with the help of DIC and post-mortem analysis. Quasi-static and dynamic crack propagations linked to this specific fracture phenomenon have been investigated by a compromised experimental setup. The setup however allowed for the investigation of the two cracking types within one fracture process. Velocity and SIF measurements obtained through DIC and Williams' series expansion have been tied to microscopic images to highlight the regime-dependent behavior of alternate cracking. By doing so, it was possible to find relationships through the synchronization of experimental devices. Main observations with potential perspectives can be summed as following:

- *'Forbidden' velocity regime.* The in literature described 'forbidden' velocity regime was not approached from two sides, but studied through holistic alternate cracking experiments with high-speed imaging. Here, the 'forbidden' regime has been identified by quasi-static and dynamic velocity threshold measurements of ∼36 cm.s^{-1} and ∼ 36 m.s^{-1}, respectively. Notice that the limit values stem from the lowest/highest measured velocity of all observed phases.

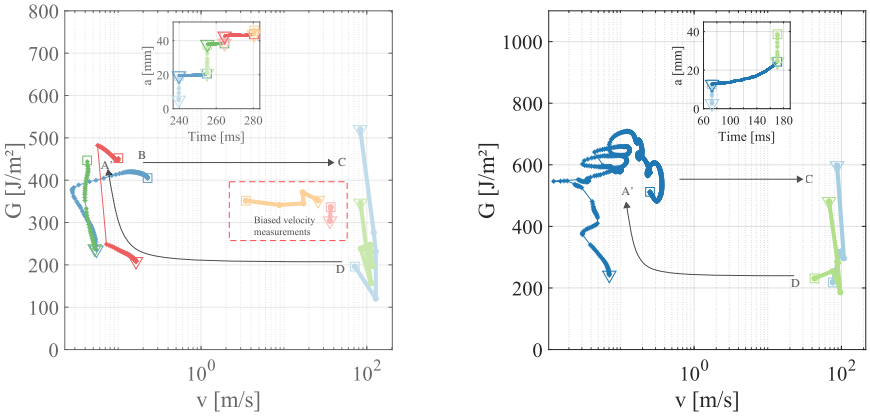

Fig. 14: Energy release rate (G) [J.m^{-2}] as a function of velocity (v) [m.s^{-1}] for the alternate cracking phases with its corresponding temporal evolution of the crack for: (a) M1-T2 and (b) M2-T19. Reference to the phases of the theoretical kinematic law (see Figure 1) are added for better comprehension.

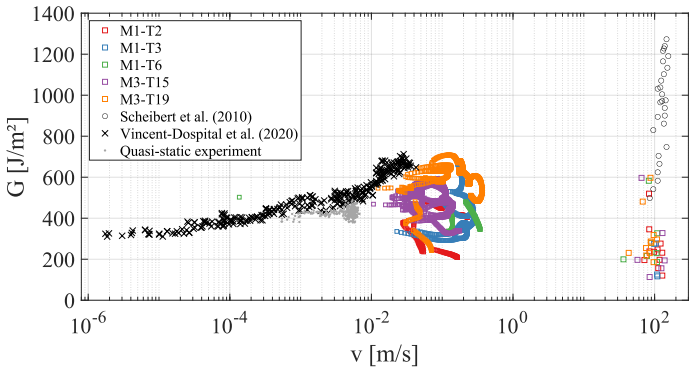

Fig. 15: Energy release rate (G) [J.m^{-2}] as a function of velocity (v) [m.s^{-1}] for the alternate cracking and one entirely quasi-static experiment.

- *Relationship of mean dynamic velocity with burst length.* Dynamic crack speeds and their burst lengths have been registered and used to establish a relationship. By doing so, it was shown that higher velocities result in longer dynamic bursts.
- *Observation of rest bands.* In line with the previous point, probably for dynamic propagation phases containing lower levels of energy, dynamic bursts show an intermittent behavior with extremely small rest bands. An average velocity threshold for the potential occurrence of rest bands has been identified at ~60 m.s^{-1}.
  Perspective: Higher temporal sampling would allow for the identification of rest band decelerations influencing the average dynamic velocity measurements and thereby the exploration of the intermittent behavior of dynamic bursts itself.

- *Deceleration phase occurring during transition of dynamic to quasi-static propagation.* The influence of dynamically propagating cracks arriving at quasi-static phase on the fracture surface led to the definition of a critical deceleration distance between the two phases. Here, an almost linear trend is found between mean crack tip speeds of the dynamic burst and the specific deceleration distance. It is found between 115 and 615 μm for mean velocities ranging from 78 to 106 m.s^{-1}. It points to the fact that the crack tip undergoes a deceleration of about 10^7 m.s^{-2}.
  Perspective: The observed extreme accelerations/decelerations potentially induce elastic waves that could be measured with Acoustic Emission (AE) devices. In that context, recent developments in Ultra High Speed (UHS) imaging techniques (temporal resolutions in the order of Mfps (Vinel et al., 2021)) would allow for a detailed investigation of the acceleration/deceleration phases and help visualizing crack induced waves propagation.
- *Particular surface markings.* Two particular PMMA-related fracture surface patterns, Wallner lines and nucleation phases, have been observed. The second one, only appearing at the beginning of the dynamic bursts, suggests crack speed phases beyond the velocities measured during the experiments. This can be explained by the limits of the chosen interframe.
  Perspective: Again, by stretching the limits of the interframe and reaching higher samplings during dynamic propagation, velocity variations could be explored. Surface markings of the nucleation phase, suggesting highest crack tip speeds in the beginning of dynamic bursts, could thereby be confirmed.
- *Improved sampling of the kinematic law of PMMA fracturing in vicinity of instability.* Kinematic law for fracturing in PMMA was established by supplementing the results of this work with experimental data from existing literature. Here, experimental data of the interaction of reoccurring dynamic and quasi-static phases during alternate cracking experiments was provided. For the first time, direct velocity and SIF measurements have been experimentally identified for both phases during the same alternate cracking experiments. Results led to a proposed adjustment of the classical description of alternate cracking regarding the transition from dynamic to quasi-static propagation (path along reference points B-C-D-A' in Figure 2.1). On one hand, in view of the chosen extension rates to induce alternate recurrence of the transitions, different mechanisms could have been activated. On the other hand, the transition of dynamic to quasi-static propagation with extreme decelerations (potentially being outside of the framework of (Vincent-Dospital et al., 2020)) is not smooth after all. In addition, the path that the crack follows to revert to the master curve in the quasi-static regime differs from the observations in (Vasudevan, 2018). However, in his work, very slow extension rates have been used resulting in quasi-static experiments initiated by a dynamic crack. No alternate recurrence of the two propagation types was observed. Regarding quasi-static to dynamic transitions, even with a temporal resolution of 40 kfps, it was not possible to experimentally explore the smooth transition during the 'softening' branch predicted by the thermodynamic model of (Vincent-Dospital et al., 2020). This, however, could potentially be explained by a lack of temporal resolution or the feasibility to explore this regime due to the way the experiments were conducted. To do so, an experimental configuration enabling decreasing K_I values with increasing crack velocities is needed.
  Perspective: An experimental configuration containing UHS imaging techniques would allow for the investigation of separate dynamic propagation phases during

alternate cracking. Consequently, better descriptions of the transition phases could be reached, potentially leading to an exploration of the predicted smooth transition, i.e. the 'softening' regime.

Acknowledgement

The authors gratefully acknowledge the support of the Agence Nationale de la Recherche (ANR) through grant ANR-19-CE42-0012.

Declarations

Conflict of interest:

The authors declare that they have no conflict of interest.

References

Ali U, Karim KJBA, Buang NA (2015) A Review of the Properties and Applications of Poly (Methyl Methacrylate) (PMMA). Polymer Reviews 55(4):678–705, DOI 10.1080/15583724.2015.1031377, URL http://www.tandfonline.com/doi/full/10.1080/15583724.2015.1031377

Atkins AG, Lee CS, Caddell RM (1975a) Time-temperature dependent fracture toughness of PMMA: Part 1. J Mater Sci 10(8):1381–1393, DOI 10.1007/BF00540829, URL http://link.springer.com/10.1007/BF00540829

Atkins AG, Lee CS, Caddell RM (1975b) Time-temperature dependent fracture toughness of PMMA: Part 2. J Mater Sci 10(8):1394–1404, DOI 10.1007/BF00540830, URL http://link.springer.com/10.1007/BF00540830

Beaumont PWR, Young RJ (1975) Failure of brittle polymers by slow crack growth: Part 1 Crack propagation in polymethylmethacrylate and time-to-failure predictions. J Mater Sci 10(8):1334–1342, DOI 10.1007/BF00540823, URL http://link.springer.com/10.1007/BF00540823

Beinert J, Kalthoff JF (1981) Experimental determination of dynamic stress intensity factors by shadow patterns. In: Sih GC (ed) Experimental evaluation of stress concentration and intensity factors, Springer Netherlands, Dordrecht, pp 281–330, DOI 10.1007/978-94-009-8337-3_5, URL http://link.springer.com/10.1007/978-94-009-8337-3_5

Besnard G, Hild F, Roux S (2006) "Finite-Element" Displacement Fields Analysis from Digital Images: Application to Portevin–Le Châtelier Bands. Exp Mech 46(6):789–803, DOI 10.1007/s11340-006-9824-8, URL http://link.springer.com/10.1007/s11340-006-9824-8

Bonamy D, Ravi-Chandar K (2003) Interaction of Shear Waves and Propagating Cracks. Phys Rev Lett 91(23):235502, DOI 10.1103/PhysRevLett.91.235502, URL https://link.aps.org/doi/10.1103/PhysRevLett.91.235502

Dally JW, Fourney WL, Irwin GR (1985) On the uniqueness of the stress intensity factor - crack velocity relationship. Int J Fract 27(3-4):159–168, DOI 10.1007/BF00017965, URL http://link.springer.com/10.1007/BF00017965

693 Dalmas D, Guerra C, Scheibert J, Bonamy D (2013) Damage mechanisms in the
694 dynamic fracture of nominally brittle polymers. Int J Fract 184(1-2):93–111,
695 DOI 10.1007/s10704-013-9839-y, URL http://link.springer.com/10.1007/
696 s10704-013-9839-y
697 Feeny B, Guran A, Hinrichs N, Popp K (1998) A Historical Review on Dry
698 Friction and Stick-Slip Phenomena. Applied Mechanics Reviews 51(5):321–
699 341, DOI 10.1115/1.3099008, URL https://asmedigitalcollection.
700 asme.org/appliedmechanicsreviews/article/51/5/321/401371/
701 A-Historical-Review-on-Dry-Friction-and-StickSlip
702 Griffith AA (1921) VI. The phenomena of rupture and flow in solids. Phil Trans
703 R Soc Lond A 221(582-593):163–198, DOI 10.1098/rsta.1921.0006, URL https://
704 royalsocietypublishing.org/doi/10.1098/rsta.1921.0006
705 Grégoire D (2008) Initiation, propagation, arrêt et redémarrage de fissures sous impact.
706 Mécanique, INSA de Lyon, URL https://theses.hal.science/tel-00418626/
707 Grégoire D, Maigre H, Combescure A (2009) New experimental and numerical tech-
708 niques to study the arrest and the restart of a crack under impact in transparent ma-
709 terials. International Journal of Solids and Structures 46(18-19):3480–3491, DOI 10.
710 1016/j.ijsolstr.2009.06.003, URL https://linkinghub.elsevier.com/retrieve/
711 pii/S0020768309002273
712 Guerra C, Scheibert J, Bonamy D, Dalmas D (2012) Understanding fast macroscale frac-
713 ture from microcrack post mortem patterns. Proc Natl Acad Sci USA 109(2):390–
714 394, DOI 10.1073/pnas.1113205109, URL https://pnas.org/doi/full/10.1073/
715 pnas.1113205109
716 Hattali M, Barés J, Ponson L, Bonamy D (2012) Low Velocity Surface Fracture Pat-
717 terns in Brittle Material: A Newly Evidenced Mechanical Instability. MSF 706-
718 709:920–924, DOI 10.4028/www.scientific.net/MSF.706-709.920, URL https://www.
719 scientific.net/MSF.706-709.920
720 Isherwood D, Williams J (1978) Some observations on the tearing of ductile materials.
721 Engineering Fracture Mechanics 10(4):887–895, DOI 10.1016/0013-7944(78)90042-5,
722 URL https://linkinghub.elsevier.com/retrieve/pii/0013794478900425
723 Kanninen MF, Popelar CH (1985) Advanced fracture mechanics. No. 15 in Oxford engi-
724 neering science series, Oxford University Press, New York
725 Lee D, Tippur H, Bogert P (2010) Quasi-static and dynamic fracture of graphite/epoxy
726 composites: An optical study of loading-rate effects. Composites Part B: En-
727 gineering 41(6):462–474, DOI 10.1016/j.compositesb.2010.05.007, URL https://
728 linkinghub.elsevier.com/retrieve/pii/S1359836810000831
729 Leevers P (1986) Crack front shape effects on propagation stability in thermoset-
730 ting polyesters. Theoretical and Applied Fracture Mechanics 6(1):45–55, DOI
731 10.1016/0167-8442(86)90049-2, URL https://linkinghub.elsevier.com/
732 retrieve/pii/0167844286900492
733 Marshall GP, Coutts LH, Williams JG (1974) Temperature effects in the fracture of
734 PMMA. J Mater Sci 9(9):1409–1419, DOI 10.1007/BF00552926, URL http://link.
735 springer.com/10.1007/BF00552926
736 Maugis D, Barquins M (1988) Stick-Slip and Peeling of Adhesive Tapes. In: Allen
737 KW (ed) Adhesion 12, Springer Netherlands, Dordrecht, pp 205–222, DOI
738 10.1007/978-94-009-1349-3_14, URL http://link.springer.com/10.1007/
739 978-94-009-1349-3_14
740 Miller O, Freund LB, Needleman A (1999) Energy dissipation in dynamic fracture of brit-
741 tle materials. Modelling Simul Mater Sci Eng 7(4):573–586, DOI 10.1088/0965-0393/

7/4/307, URL https://iopscience.iop.org/article/10.1088/0965-0393/7/4/307

Ravi-Chandar K, Balzano M (1988) On the mechanics and mechanisms of crack growth in polymeric materials. Engineering Fracture Mechanics 30(5):713–727, DOI 10.1016/0013-7944(88)90161-0, URL https://linkinghub.elsevier.com/retrieve/pii/0013794488901610

Ravi-Chandar K, Yang B (1997) On the role of microcracks in the dynamic fracture of brittle materials. Journal of the Mechanics and Physics of Solids 45(4):535–563, DOI 10.1016/S0022-5096(96)00096-8, URL https://linkinghub.elsevier.com/retrieve/pii/S0022509696000968

Rohatgi A (2022) Webplotdigitizer: Version 4.6. URL https://github.com/ankitrohatgi/WebPlotDigitizer

Roux S, Hild F (2006) Stress intensity factor measurements from digital image correlation: post-processing and integrated approaches. Int J Fract 140(1-4):141–157, DOI 10.1007/s10704-006-6631-2, URL http://link.springer.com/10.1007/s10704-006-6631-2

Roux-Langlois C, Gravouil A, Baietto MC, Réthoré J, Mathieu F, Hild F, Roux S (2015) DIC identification and X-FEM simulation of fatigue crack growth based on the Williams' series. International Journal of Solids and Structures 53:38–47, DOI 10.1016/j.ijsolstr.2014.10.026, URL https://linkinghub.elsevier.com/retrieve/pii/S0020768314004053

Réthoré J (2015) Automatic crack tip detection and stress intensity factors estimation of curved cracks from digital images: Automatic crack tip detection and SIF estimation of curved cracks. Int J Numer Meth Engng 103(7):516–534, DOI 10.1002/nme.4905, URL https://onlinelibrary.wiley.com/doi/10.1002/nme.4905

Réthoré J (2018) UFreckles. DOI 10.5281/ZENODO.1433776, URL https://zenodo.org/record/1433776, language: en

Réthoré J, Roux S, Hild F (2011) Optimal and noise-robust extraction of Fracture Mechanics parameters from kinematic measurements. Engineering Fracture Mechanics 78(9):1827–1845, DOI 10.1016/j.engfracmech.2011.01.012, URL https://linkinghub.elsevier.com/retrieve/pii/S0013794411000312

Scheibert J, Guerra C, Célarié F, Dalmas D, Bonamy D (2010) Brittle-Quasibrittle Transition in Dynamic Fracture: An Energetic Signature. Phys Rev Lett 104(4):045501, DOI 10.1103/PhysRevLett.104.045501, URL https://link.aps.org/doi/10.1103/PhysRevLett.104.045501

Vasudevan A, Grabois TM, Cordeiro GC, Morel S, Filho RDT, Ponson L (2021) Adaptation of the tapered double cantilever beam test for the measurement of fracture energy and its variations with crack speed. arXiv preprint arXiv:210104380 DOI 10.48550/ARXIV.2101.04380, URL https://arxiv.org/abs/2101.04380, publisher: arXiv Version Number: 1

Vasudevan AV (2018) Deciphering triangular fracture patterns in PMMA : how crack fragments in mixed mode loading. PhD thesis, Sorbonne University, URL https://tel.archives-ouvertes.fr/tel-02180510

Vincent-Dospital T, Toussaint R, Santucci S, Vanel L, Bonamy D, Hattali L, Cochard A, Flekkøy EG, Måløy KJ (2020) How heat controls fracture: the thermodynamics of creeping and avalanching cracks. Soft Matter 16(41):9590–9602, DOI 10.1039/D0SM01062F, URL http://xlink.rsc.org/?DOI=D0SM01062F

Vinel A, Seghir R, Berthe J, Portemont G, Réthoré J (2021) Metrological assessment of multi-sensor camera technology for spatially-resolved ultra-high-speed imaging of

transient high strain-rate deformation processes. Strain 57(4), DOI 10.1111/str.12381, URL https://onlinelibrary.wiley.com/doi/10.1111/str.12381

Wallner, H (1939) H. Wallner. Z. Phys. 114, 368

Wang PP, Lee S, Harmon JP (1994) Ethanol-induced crack healing in poly(methyl methacrylate). J Polym Sci B Polym Phys 32(7):1217–1227, DOI 10.1002/polb.1994.090320709, URL https://onlinelibrary.wiley.com/doi/10.1002/polb.1994.090320709

Williams ML (1957) On the Stress Distribution at the Base of a Stationary Crack. Journal of Applied Mechanics 24(1):109–114, DOI 10.1115/1.4011454, URL https://asmedigitalcollection.asme.org/appliedmechanics/article/24/1/109/1110895/On-the-Stress-Distribution-at-the-Base-of-a

Yamini S, Young R (1977) Stability of crack propagation in epoxy resins. Polymer 18(10):1075–1080, DOI 10.1016/0032-3861(77)90016-7, URL https://linkinghub.elsevier.com/retrieve/pii/0032386177900167